Scilight

Journal of Innovations in Materials and Manufacturing Engineering
https://www.sciltp.com/journals/jimme



Article

Check for updates

Tribological Behavior of Ti-6Al-4V Alloys Processed by Selective Laser Melting and Conventional Casting Process

Anil Kumar Chaubey [1], Sameer Sahoo [1] and K. G. Prashanth [2,3,4,*]

[1] CSIR-Institute of Minerals and Materials Technology (CSIR-IMMT), Bhubaneswar 751013, India
[2] National Engineering Research Center of Near-net-shape Forming for Metallic Materials, South China University of Technology, Guangzhou 510641, China
[3] Department of Mechanical and Industrial Engineering, Tallinn University of Technology, Ehitajate tee 5, 19086 Tallinn, Estonia
[4] Department of Biosciences, Saveetha School of Engineering, Saveetha Institute of Medical and Technical Sciences, Chennai 602117, India
* Correspondence: kgprashanth@gmail.com

How To Cite: Chaubey, A.K.; Sahoo, S.; Prashanth, K.G. Tribological Behavior of Ti-6Al-4V Alloys Processed by Selective Laser Melting and Conventional Casting Process. *Journal of Innovations in Materials and Manufacturing Engineering* **2026**, *1*(1), 8. https://doi.org/10.53941/jimme.2026.100008

Received: 15 September 2026
Revised: 22 October 2026
Accepted: 25 October 2026
Published: 6 November 2026

Abstract: This work presents a detailed assessment of the microstructural features and tribological behaviour of Ti-6Al-4V alloy produced by conventional casting followed by rolling (CR) and selective laser melting (SLM). The two fabrication routes yield markedly different microstructures: the CR alloy develops a dual-phase α + β microstructure, whereas the SLM alloy forms a fine martensitic α′ lath morphology with enhanced hardness. Tribological experiments performed under various loads and sliding speeds reveal clear distinctions in frictional response and wear characteristics. The CR samples exhibit deeper ploughing grooves, stronger oxidation effects, and higher coefficients of friction, indicating that abrasive and oxidation-assisted wear dominate their surface degradation. In contrast, the SLM samples show shallower wear tracks, reduced friction, and improved resistance to material removal, with delamination and adhesive wear occurring only under more severe test conditions. The lower COF and diminished wear severity observed in the SLM alloy highlight the advantages of its refined microstructure in stabilizing interfacial contact and reducing frictional energy losses. Overall, the results confirm the superior tribological performance of SLM-processed Ti-6Al-4V for applications demanding high wear resistance and structural reliability.

Keywords: additive manufacturing; laser powder bed fusion; Ti-6Al-4V; tribology; wear properties

1. Introduction

Ti-6Al-4V is one of the most widely used α + β titanium alloys and has become a cornerstone material in several high-performance engineering sectors. Its exceptional combination of high specific strength, good fracture toughness, excellent corrosion resistance, and biocompatibility has enabled its extensive use in aerospace structures, pressure vessels, aircraft turbine and compressor blades, discs, and a wide range of surgical and orthopedic implants [1–3]. The alloy's relatively low density and ability to retain strength at moderately elevated temperatures further enhance its suitability for components where weight reduction and reliability are critical. In addition, Ti-6Al-4V exhibits good environmental stability, making it attractive for service in chemically aggressive or humid environments.

Despite these advantages, Ti-6Al-4V also possesses several intrinsic shortcomings that limit its broader application potential. Its relatively low hardness and strong tendency for adhesion during sliding contact result in

Copyright: © 2026 by the authors. This is an open access article under the terms and conditions of the Creative Commons Attribution (CC BY) license (https://creativecommons.org/licenses/by/4.0/).
Publisher's Note: Scilight stays neutral with regard to jurisdictional claims in published maps and institutional affiliations.

poor wear resistance, which restricts its use in tribologically demanding environments [4,5]. The alloy's inherently low thermal conductivity leads to localized heat accumulation during machining or frictional loading, contributing to rapid tool wear and surface damage. Furthermore, Ti-6Al-4V exhibits modest fatigue resistance, particularly under cyclic loading conditions involving stress concentrations or complex loading paths [6]. These limitations become more pronounced in applications requiring long service life, high surface durability, or efficient heat dissipation. Additional challenges such as poor shear strength, limited resistance to fretting, and difficulties in achieving high-quality surface finishes further constrain its performance envelope [5].

Additive manufacturing (AM), also referred to as 3D printing or rapid prototyping, is a layer-by-layer fabrication approach that builds components directly from digital 3D model data, in contrast to conventional subtractive manufacturing methods [7–9]. Among various AM technologies, laser powder-bed fusion (LPBF), also known as selective laser melting (SLM), is a powder-bed fusion-based process widely used for producing metallic parts with enhanced functionalities [10–12]. Owing to its highly localized laser-powder interaction and precise thermal control, SLM enables the fabrication of near-fully dense components with excellent dimensional accuracy and improved mechanical and tribological performance [13–17].

Titanium and its alloys, despite their attractive combination of mechanical strength, chemical stability, and low density (4.5 g/cm^3), exhibit inherently poor wear resistance, which restricts their use in demanding structural and tribological applications [18]. The inadequate tribological performance of Ti-based alloys arises primarily from two factors. First, their low resistance to plastic shearing and limited work-hardening capability mean that wear mechanisms governed by mechanical properties, such as adhesion, abrasion, and delamination, are insufficiently counteracted by the material [3]. Second, the protective surface oxide formed during dry sliding is unable to withstand the high flash temperatures generated at the contact interface. This oxide layer is prone to spalling and micro-fragmentation, offering minimal protection to the underlying subsurface against wear. Furthermore, oxygen dissolved from the surrounding atmosphere can diffuse into the matrix, causing embrittlement and reducing the overall mechanical integrity of the alloy [19].

Due to the formation of a refined microstructure containing hard martensitic phases, the wear performance of Ti-based alloys such as Ti-6Al-4V can be markedly improved when processed using advanced additive manufacturing techniques like LPBF/SLM. Motivated by this potential enhancement, the present study aims to systematically investigate and compare the microstructure, mechanical properties, and wear behavior of Ti-6Al-4V alloys fabricated through conventional casting and selective laser melting. This comparative assessment may provide insight into the extent to which SLM-induced microstructural refinement contributes to improved functional performance relative to traditionally processed counterparts.

2. Experimental Details

Argon-atomized commercially pure Ti-6Al-4V (Grade 5) powder with a spherical morphology was used in this study. Cylindrical rods with a diameter of 10 mm and a length of 100 mm were fabricated using both conventional casting and selective laser melting (SLM). The conventionally cast samples were subsequently subjected to rolling to enhance their microstructure and properties. The SLM specimens were produced using a ReaLizer SLM-50 system equipped with a fibre laser capable of delivering up to 120 W of power, with a laser spot size of approximately 39 μm. The processing parameters employed included a hatch spacing of 60 μm, a scanning speed of 1000 mm/s, a layer thickness of 25 μm, and a hatch rotation of 73°. A single-track straight-line scanning strategy was adopted. All builds were carried out on a 20 mm-thick Ti substrate plate under a high-purity argon atmosphere containing less than 0.02% oxygen to minimize oxidation during processing. All the structural and microstructural characterization and the frictional and wear properties were measured along the cross-section of the sample taken along the building direction.

The microstructure of the specimens, prepared by standard metallographic polishing followed by etching with Kroll's reagent (5 mL HNO_3, 3 mL HF, and 100 mL distilled water), was examined using an optical microscope (OM) (Leica DMI3000M). Surface morphology was characterized using a field-emission scanning electron microscope (FE-SEM; Carl Zeiss Supra 55), and elemental analysis was performed with the attached energy-dispersive X-ray spectroscopy (EDS) system. Phase identification was carried out using X-ray diffraction (XRD) on a Rigaku SmartLab SE diffractometer equipped with a Cu-Kα radiation source (λ = 1.54 Å), operated at a scanning speed of 2°/min. The resulting diffraction patterns were analyzed using X'Pert HighScore Plus software. The density (ρ) of the specimens was measured according to Archimedes' principle using distilled water as the immersion medium. Three randomly selected samples were evaluated, and all mass measurements were performed using an electronic balance with an accuracy of ±0.0001 g. Hardness testing was conducted on polished specimens using a Vickers microhardness tester (LECO LM247). A load of 100 gf and a dwell time of 13 s were

consistently applied throughout the measurements. For each specimen, five microhardness indentations were performed at different locations on the test surface, and the reported value was calculated as the arithmetic mean of the individual measurements.

Dry sliding wear tests were performed using a pin-on-disc apparatus (Wear & Friction Monitor, Model TR-20) under ambient laboratory conditions at a temperature of (35 ± 2) °C and relative humidity (62.5 ± 1) %. During testing, the Ti-6Al-4V pins polished using abrasive paper (600 grit) were pressed against the counter face of a rotating EN31 steel disc with a wear track diameter of 60 mm. The EN31 steel disc has a hardness of 61 HRC and was polished using abrasive paper prior to testing. Experiments were conducted under normal loads of 30, 40, 50, 80, and 100 N at sliding velocities of 0.5, 1.0, 1.5, 2.0, and 2.5 m/s. The pin specimens measured 30–35 mm in length and 8 mm in diameter. Parameters such as rotational speed, test duration, and rpm were kept constant for all trials. The wear rate was calculated using the following equation [20]:

$$Q_S = \frac{V_S}{L_S} \tag{1}$$

where Q_s is the wear rate, V_s is the sliding volume loss and L_s is the sliding distance. The initial surface roughness parameters are not measured for both SLM and cast samples, and it may influence the frictional and wear behavior, however, the trend is expected to be similar. The volume loss was determined from the mass loss of the flat-head pins, measured before and after each test. The sliding distance was calculated using the following relationship:

$$L_s = 2\pi\, r_s\, v_s\, t_s \tag{2}$$

where, r_s is the radius of the wear track (22.5 mm), v_s is the rotational speed (240 rpm) and t_s is the test duration (15 min). The worn sample surface examined using OM and FESEM equipped with an EDS system to elucidate the prevailing wear mechanisms. To ensure the reliability and reproducibility of the experimental results, each testing condition was evaluated using three independent replicate tests. The coefficient of friction (COF) was continuously recorded during each test, and the wear rate was subsequently determined. The reported results represent the mean values of the three replicate measurements.

3. Results and Discussion

3.1. Structural and Microstructural Characterization

The XRD patterns of the Ti-6Al-4V alloys fabricated by conventional casting followed by rolling (CR) and by SLM are presented in Figure 1. The conventionally processed CR sample exhibits predominantly α-Ti peaks corresponding to the hexagonal close-packed (hcp) phase. A weak peak at a scattering angle of ~39.5° is also observed, which corresponds to the β-Ti phase with a body-centered cubic (bcc) structure. This indicates the presence of a small volume fraction of β-Ti, consistent with the Ti-6Al-4V phase diagram, as the alloy is a dual-phase α + β system [21].

The XRD pattern of the SLM-processed alloy is similar in overall peak positions, showing reflections characteristic of the hcp phase. However, no distinct β-Ti peak is detected. This may be due to overlap of β-phase reflections with the α-phase peaks or the presence of β-Ti in very low quantities (below ~5%, the typical detection limit of XRD), and therefore its presence cannot be conclusively confirmed from the diffraction pattern [22]. Based on prior studies, the dominant hcp reflections in the SLM sample are attributed to the formation of martensitic α′, which develops due to the extremely high cooling rates inherent to the SLM process [23–26]. The formation of α′ martensite is further supported by the rapid solidification conditions associated with laser melting and subsequent cooling [27,28].

In addition, the XRD peaks of the SLM sample exhibit noticeable broadening compared to the CR counterpart. This broadening can be attributed to the significantly higher defect density in the SLM alloy (dislocation density: $3.5 \pm 1.0 \times 10^{15}$ m^{-2}) relative to the CR sample ($6.2 \pm 1.8 \times 10^{13}$ m^{-2}). The high internal strain generated during rapid cooling, combined with the refined microstructure (crystallite size ~15.3 nm for SLM vs. ~93 nm for CR), also contributes to the observed peak broadening.

Figure 2 presents the OM and FESEM micrographs of the Ti-6Al-4V samples fabricated by both CR and SLM processes. Clear differences in microstructural features are evident, primarily due to the distinct thermal histories associated with each processing route, particularly variations in cooling rate and solidification mode. The SLM-processed sample contains visible micropores (<1 μm), whereas the CR sample shows no detectable porosity in the OM images Figure 2a,c. The relative densities measured using Archimedes' method are 99.7% for the CR sample and 99.0% for the SLM sample (theoretical density of Ti-6Al-4V taken as 4.43 g/cm^3). The CR specimen exhibits a typical dual-phase microstructure comprising α-Ti (stabilized by Al) and β-Ti (stabilized by V),

consistent with the XRD results (Figure 2a,b). The α phase appears grey, while the β phase appears bright. A lamellar morphology is observed, with β lamellae of average thickness ~0.85 μm located along the α-phase boundaries (Figure 2b).

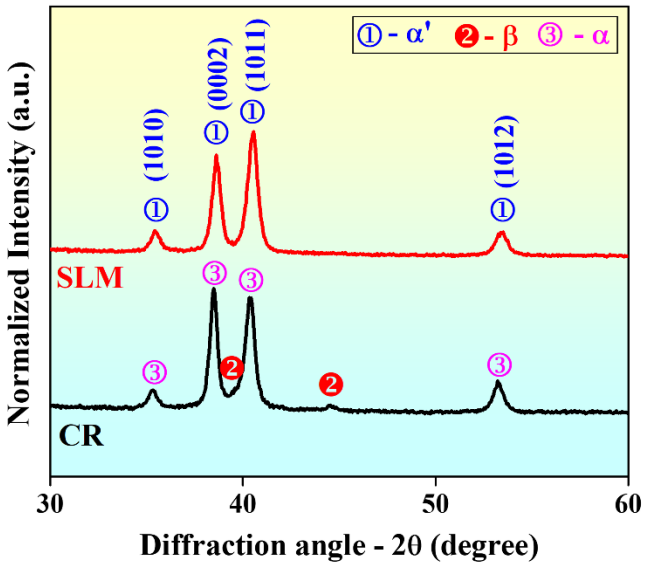


Figure 1. X-ray diffraction (XRD) patterns (Cu-Kα radiation) of Ti-6Al-4V samples fabricated by conventional casting followed by rolling (CR) and by selective laser melting (SLM). The diffraction profiles highlight clear differences in the phases present in the two processing conditions.

In contrast, the SLM-processed sample exhibits a distinctly different microstructure and phase constitution compared to its CR counterpart (Figure 2c,d). It is characterized by long, slender laths typical of the α′-martensitic structure (Figure 2d). The formation of such α′-martensitic laths is attributed to the extremely high cooling rates inherent to the SLM process, often reaching the order of 10^5–10^6 °C/s [29]. The α′ laths in the present study measure ~0.3 μm in width and ~8 μm in length, reflecting the rapid solidification and diffusion-limited transformation associated with the SLM process.

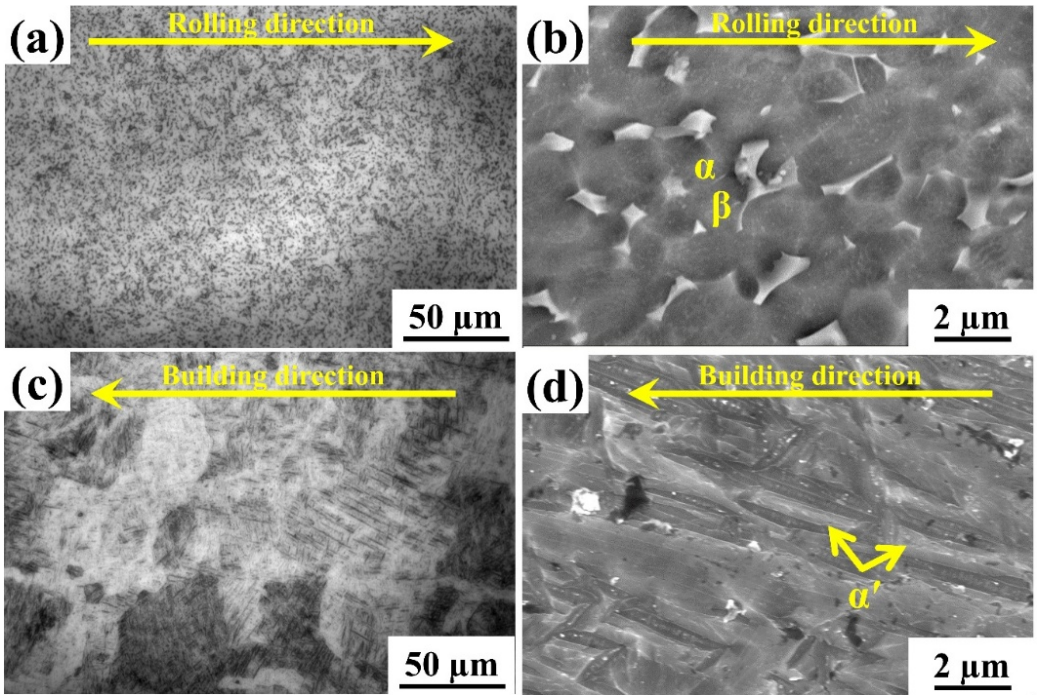


Figure 2. Optical microscopy (OM) and field-emission scanning electron microscopy (FESEM) cross-sectional images of Ti-6Al-4V samples fabricated by (**a**,**b**) conventional casting followed by rolling (CR) and (**c**,**d**) selective laser melting (SLM), highlighting distinct differences in phase constituents and microstructural morphology.

3.2. Hardness Measurements

Figure 3 presents the microhardness values of the Ti-6Al-4V samples fabricated by CR and SLM. The CR sample exhibits a hardness of 314 ± 25 HV, whereas the SLM-processed counterpart shows a significantly higher hardness of 392 ± 18 HV. The enhanced hardness of the SLM sample can be attributed to several factors: (1) a markedly higher internal defect density, particularly dislocations ($3.5 \pm 1.0 \times 10^{15}$ m^{-2} for SLM vs. $6.2 \pm 1.8 \times 10^{13}$ m^{-2} for CR); (2) a substantially finer crystallite size (~15.3 nm for SLM compared to ~93 nm for CR); and (3) the presence of a hard α′-martensitic microstructure in the SLM sample, in contrast to the relatively softer α + β dual-phase microstructure observed in the CR counterpart.

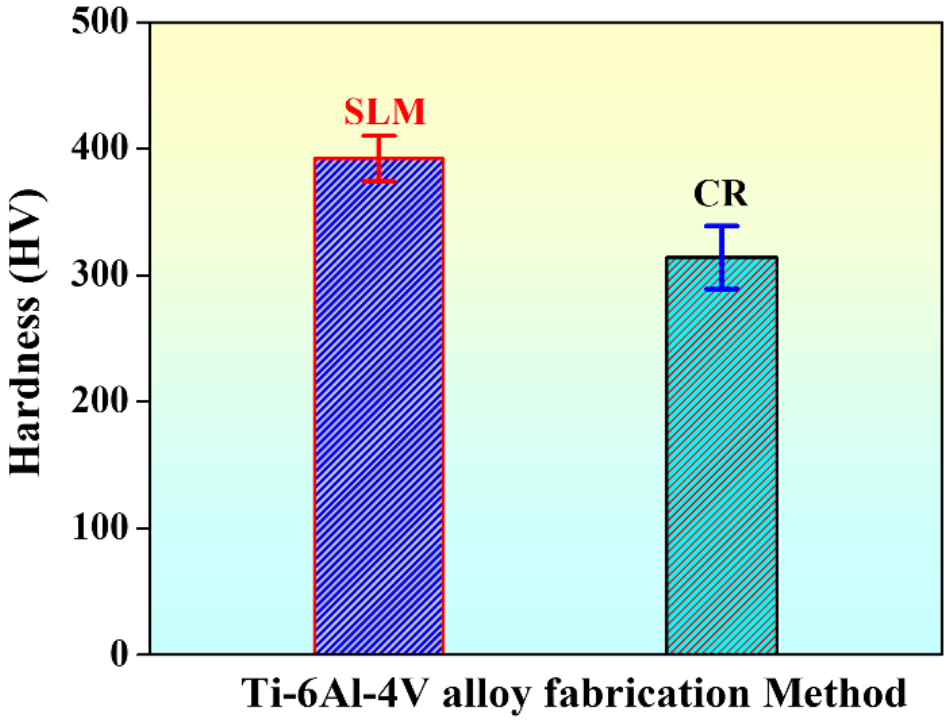


Figure 3. Microhardness values of Ti-6Al-4V samples fabricated by conventional casting followed by rolling (CR) and by selective laser melting (SLM), illustrating the differences in hardness arising from the two processing routes.

3.3. Wear Behaviour

Figure 4 presents the wear rate of Ti-6Al-4V samples fabricated by CR and SLM under varying tribological conditions. It is evident from the plot that the processing route exerts a pronounced influence on the wear performance of the alloy. Across all tested conditions, the SLM-processed sample consistently exhibits a lower wear rate compared to its CR counterpart, demonstrating superior wear resistance. This improvement can be directly linked to the higher hardness of the SLM sample, which arises from its refined microstructure, elevated dislocation density, and the presence of hard α′-martensitic laths. The formation of α′ martensite during SLM, driven by extremely high cooling rates, contributes significantly to the enhanced resistance against plastic deformation and material removal during sliding, thereby reducing the wear rate [18].

The trends observed in Figure 4 further show that the wear rate increases almost linearly with increasing sliding speed (from 0.5 m/s to 2.5 m/s) at a constant load of 40 N, as well as with increasing load (from 30 N to 100 N) at a constant sliding speed of 0.5 m/s for both CR and SLM samples. This behaviour is typical of metallic systems subjected to dry sliding conditions. As sliding speed increases, frictional heating at the contact interface intensifies, leading to a rise in contact temperature [30,31]. Elevated temperatures promote softening of the surface layers, accelerate oxidation, and increase the propensity for material removal, thereby elevating the wear rate [32,33]. Similarly, higher applied loads increase the real area of contact and the severity of asperity interactions, resulting in greater material loss [34]. Despite these effects, the SLM sample maintains a consistently lower wear rate, underscoring the beneficial role of its martensitic microstructure in improving tribological performance [18].

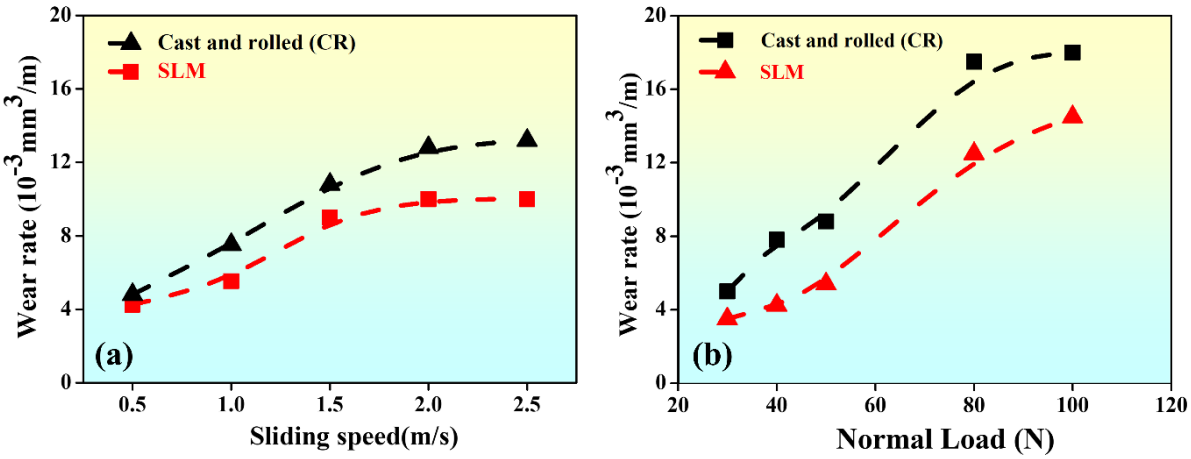


Figure 4. Wear rate of Ti-6Al-4V samples measured under (**a**) a constant load of 40 N with sliding speeds varying from 0.5 m/s to 2.5 m/s, and (**b**) a constant sliding velocity of 0.5 m/s with applied loads ranging from 30 N to 100 N.

The worn surfaces of the Ti-6Al-4V samples fabricated by CR and SLM and tested against a hard steel disc were examined using FESEM, and the corresponding wear tracks are presented in Figure 5. The sliding direction in each micrograph is indicated by arrows. Figure 5a–c show the worn surfaces of the CR sample under applied loads of 50 N, 40 N, and 30 N, respectively and at a slow sliding speed of 0.5 m/s. The images reveal that material removal in the CR sample occurs predominantly through ploughing action. Ploughing refers to the displacement of material to the sides of an abrasion groove without complete removal from the surface [35]. Both the depth and width of the ploughing grooves increase with applied load, with groove depth rising from approximately 2 µm to ~5 µm and groove width increasing from ~15 µm to ~38.5 µm as the load increases from 30 N to 50 N. The presence of these grooves aligned with the sliding direction confirms abrasive wear as the dominant wear mechanism [36,37]. Additionally, oxide particles are observed along the wear track, indicating the concurrent operation of an oxidation-assisted wear mechanism [38,39]. A considerable amount of wear debris is also accumulated along the edges of the ploughing grooves, further reflecting the severity of material removal under higher loads Figure 5a–c [40].

In contrast, the worn surfaces of the SLM samples (Figure 5d–f) exhibit much shallower ploughing grooves under applied loads of 40 N and 50 N, with groove widths of approximately 13 µm and 15 µm and groove depths of <1 µm and ~1.1 µm, respectively. At the higher load of 50 N, signs of delamination are also evident, indicating localized subsurface crack initiation and subsequent detachment of material layers [41]. The SLM sample tested under the lower load of 30 N does not show pronounced ploughing grooves; instead, the surface remains comparatively smooth. However, the presence of galling marks suggests adhesive interaction between the sliding surfaces, likely arising from localized junction formation and tearing during sliding [42,43]. Overall, the dominant wear mechanisms in the SLM samples at 40 N and 50 N are abrasive wear accompanied by delamination, whereas at 30 N the wear behaviour is governed primarily by adhesive wear [44]. The differences in weight loss and the associated wear mechanisms observed in the CR and SLM samples can be attributed to variations in their hardness and the distinct deformation processes governed by their respective microstructural characteristics.

At the higher sliding speed of 1 m/s, the deep grooves observed at lower speeds transform into shallow scratches and grooves accompanied by extensive plastic deformation (Figure 6). In addition, some delamination cracks have developed along the ploughing grooves [45], indicating subsurface damage initiated by intensified shear stresses. The increase in sliding speed also raises the interfacial temperature due to enhanced frictional heating [46–48], promoting oxidation; consequently, oxide particles are evident on the worn surface of the CR sample (Figure 6b). Micro-fragmentation of these fine oxide particles is also visible in Figure 6b. In contrast, the SLM sample exhibits signs of delamination [41,49] along with shallow ploughing grooves, resulting in a relatively rough surface morphology (Figure 6c,d).

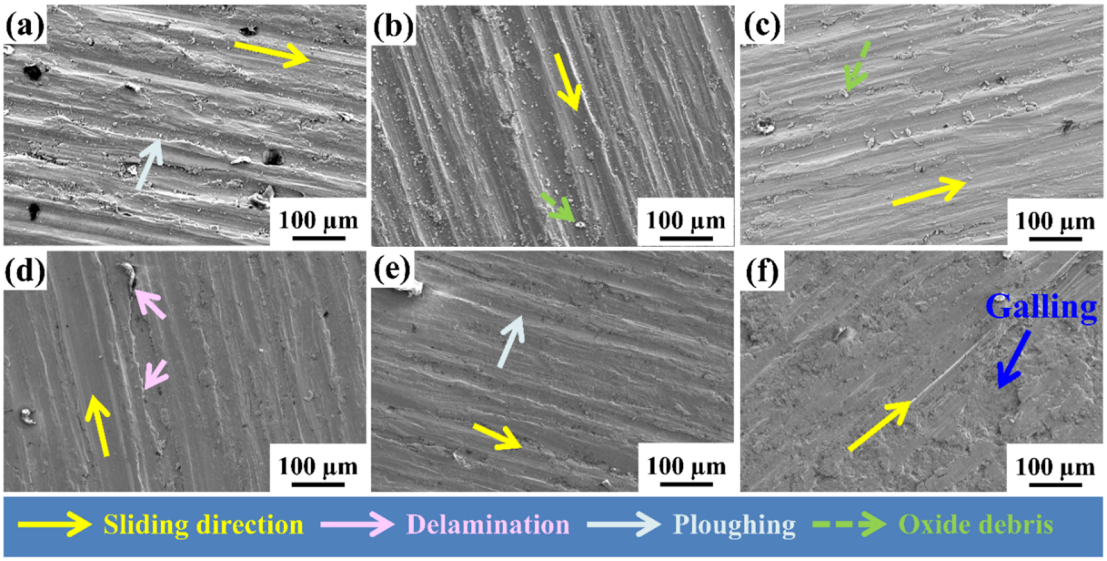


Figure 5. Field-emission scanning electron microscopy (FESEM) images of Ti-6Al-4V samples after wear testing under applied loads of 50 N, 40 N, and 30 N at a sliding speed of 0.5 m/s. Images (**a**–**c**) correspond to the cast and subsequently rolled (CR) samples, while images (**d**–**f**) depict the selective laser melted (SLM) samples. The FESEM micrographs clearly reveal the distinct differences in wear-damage severity between the CR and SLM samples.

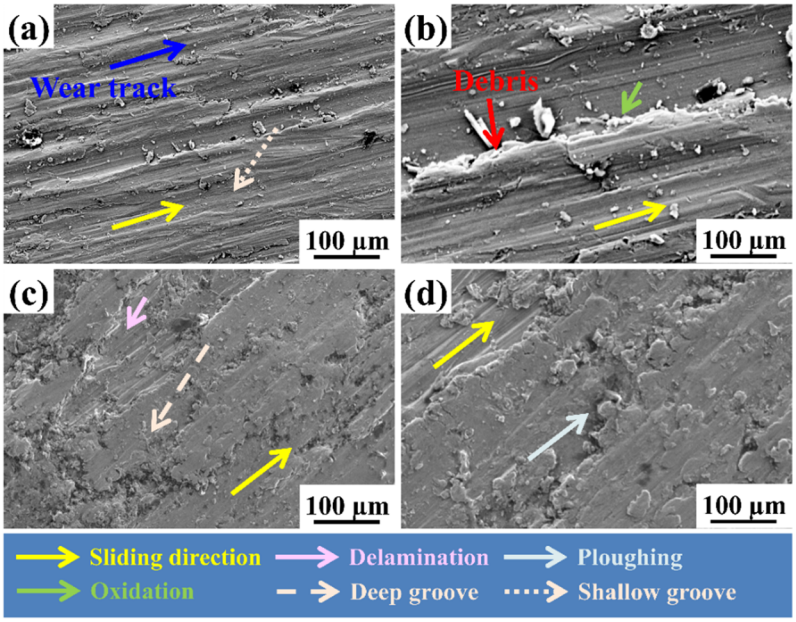


Figure 6. Field-emission scanning electron microscopy (FESEM) images of Ti-6Al-4V samples after wear testing at an applied load of 40 N at a sliding speed of 1 m/s. Images (**a**,**b**) correspond to the cast and subsequently rolled (CR) samples, while images (**c**,**d**) depict the selective laser melted (SLM) samples at both low and high magnifications. The FESEM micrographs clearly reveal the distinct differences in wear-damage severity between the CR and SLM samples.

The FESEM images of Ti-6Al-4V samples tested at an applied load of 40 N under sliding speeds of 0.5 m/s, 1 m/s, and 1.5 m/s, respectively are shown in Figure 7. In the CR samples, pronounced ploughing is observed, indicating abrasive wear as the dominant mechanism [36,37], accompanied by oxidation-assisted wear [38,39] (see Table 1). The ploughing grooves become progressively deeper and wider as the sliding speed increases from 0.5 m/s to 1.5 m/s along with a corresponding increase in oxidation (Figure 7a–c). In contrast, the worn surfaces of the SLM samples exhibit much shallower ploughing grooves, although their volume increases with sliding speed (0.5 m/s, 1 m/s, and 1.5 m/s) under the same applied load of 40 N (Figure 7d–f). At the highest sliding speed (1.5 m/s) signs of oxidation (see Table 1) and delamination become evident, indicating that abrasive and oxidative wear mechanisms dominate in the SLM samples (Figure 7f).

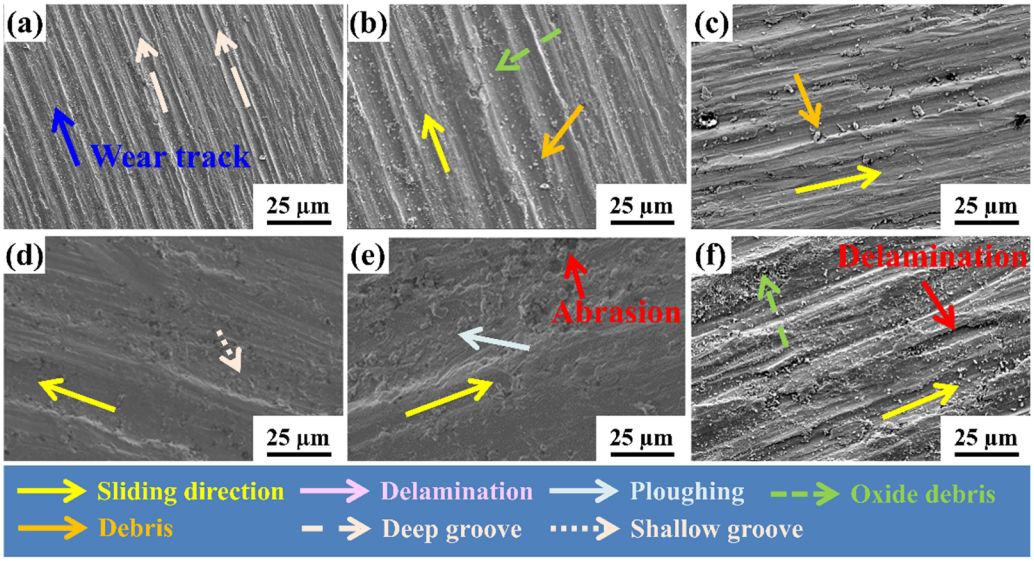


Figure 7. Field-emission scanning electron microscopy (FESEM) images of Ti-6Al-4V samples after wear testing at an applied load of 40 N and at varying sliding speeds: 0.5 m/s, 1 m/s, and 1.5 m/s, respectively. Images (**a**–**c**) correspond to the cast and subsequently rolled (CR) samples, while images (**d**–**f**) depict the selective laser melted (SLM) samples. The FESEM micrographs clearly reveal the distinct differences in wear-damage severity between the CR and SLM samples.

The evolution of the coefficient of friction (COF) for the Ti-6Al-4V samples fabricated by CR and SLM as a function of sliding distance is presented in Figure 8. The COF in metallic systems is influenced by several factors, including material composition, phase constitution, microstructural features, surface roughness and texture, environmental conditions, applied load, sliding speed, and sliding distance [50,51]. For both samples, the COF stabilizes rapidly after a short running-in period, indicating the establishment of a steady tribological interface.

Table 1. Shows the EDS analysis (in wt.%) of the Ti-6Al-4V sample surfaces fabricated by casting followed by rolling (CR) and by selective laser melting (SLM), performed before and after the wear tests.

Fabrication Method	Condition	Ti	Al	V	O	Fe
Casting and subsequent rolling (CR)	Surface before wear	90.50 ± 1.20	5.00 ± 1.80	3.80 ± 0.60	0.14 ± 0.07	0.07 ± 0.02
	Surface after wear	83.00 ± 7.20	4.80 ± 2.80	3.80 ± 2.80	4.50 ± 2.50	3.80 ± 1.60
Selective laser melting (SLM)	Surface before wear	89.80 ± 1.30	5.80 ± 0.12	3.80 ± 0.80	0.12 ± 0.06	0.48 ± 0.03
	Surface after wear	79.90 ± 6.30	6.60 ± 2.50	3.70 ± 0.19	5.60 ± 2.30	4.20 ± 1.80

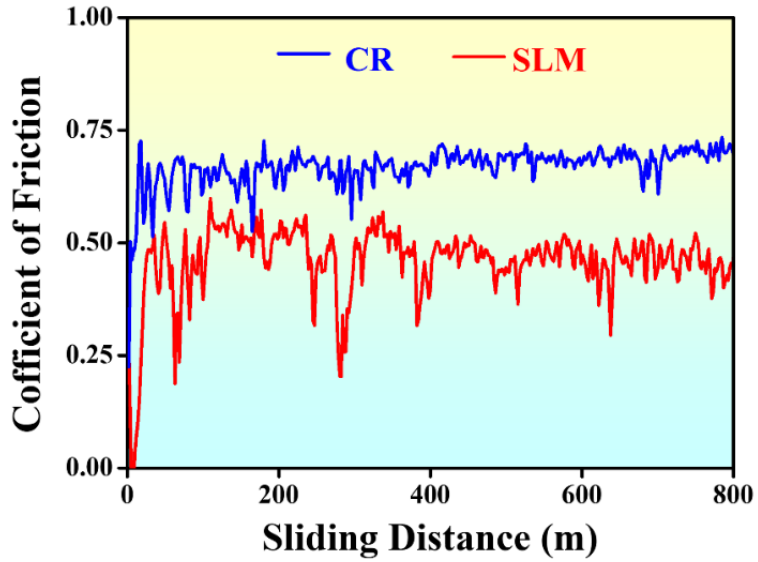


Figure 8. Friction-coefficient plot for Ti-6Al-4V samples fabricated by conventional casting followed by rolling (CR) and by selective laser melting (SLM), obtained under a normal load of 40 N and a sliding speed of 1 m/s.

The CR sample exhibits a higher steady-state COF of approximately 0.6 ± 0.1 (no unit), whereas the SLM sample shows a lower COF of about 0.4 ± 0.2 (no unit). These values are in good agreement with previously reported frictional behaviour of Ti-6Al-4V produced through similar manufacturing routes [16,50]. The higher COF observed in the CR sample suggests increased interfacial shear resistance and greater frictional energy dissipation, typically associated with reduced wear resistance. In contrast, the lower COF of the SLM sample reflects smoother interfacial sliding, likely arising from its refined microstructure and higher hardness, which collectively reduce adhesive interactions and ploughing contributions. Consequently, the SLM sample is expected to exhibit superior wear resistance (reduced wear rate) compared to the CR counterpart, consistent with the wear-rate trends observed in this study.

4. Conclusions

This study provides a comprehensive evaluation of the microstructural characteristics and tribological performance of Ti-6Al-4V alloy fabricated through conventional casting followed by rolling (CR) and selective laser melting (SLM). The two processing routes produced distinctly different microstructures: the CR alloy exhibited a relatively course α + β microstructure, whereas the SLM alloy developed a refined martensitic α′ lath microstructure with significantly higher hardness. These structural differences governed the deformation behaviour, frictional response, and wear mechanisms under varying loads and sliding speeds.

Tribological testing revealed that the CR samples experienced pronounced ploughing, deeper wear grooves, higher oxidation tendency, and elevated coefficients of friction. Abrasive and oxidation-assisted wear dominated across all test conditions, reflecting the lower hardness and reduced resistance to plastic deformation of the CR microstructure. In contrast, the SLM samples displayed shallower ploughing grooves, reduced friction, and improved resistance to material removal. Delamination and adhesive wear appeared only at higher loads and sliding speeds, highlighting the stability of the SLM microstructure under moderate tribological conditions. The lower COF and reduced severity of wear features in the SLM samples underscore the beneficial influence of their refined microstructure, which enhances interfacial stability, suppresses severe plastic deformation, and minimizes frictional energy dissipation. Variations in sliding speed further revealed transitions in wear morphology, yet the extent of damage remained consistently lower in the SLM alloy.

Overall, the findings demonstrate that SLM-processed Ti-6Al-4V exhibits superior wear resistance and more stable frictional behaviour than its CR counterpart, making it a promising candidate for applications requiring enhanced tribological performance and structural reliability.

Author Contributions

A.K.C.—Conceptualization, methodology, data curation, investigation, formal analysis, writing—original draft; S.S.—Experiments, data curation, investigation, formal analysis, writing—original draft; K.G.P.—Conceptualization, validation, resources, supervision, project administration, funding acquisition, writing—review and editing. All authors have read and agreed to the published version of the manuscript.

Funding

This work was supported by the European Union through the REFRESH – Research Excellence for Region Sustainability and High-tech Industries project (CZ.10.03.01/00/22_003/0000048) via the Operational Programme Just Transition. The research was also funded under project No. CZ.02.01.01/00/22_008/0004631, Materials and Technologies for Sustainable Development, within the Jan Amos Komenský Operational Programme, co-financed by the European Union and the Ministry of Education, Youth and Sports of the Czech Republic.

Institutional Review Board Statement

Not Applicable.

Informed Consent Statement

Not Applicable.

Data Availability Statement

Data may be made available at reasonable request to the authors.

Conflicts of Interest

The authors declare no potential conflict of interest.

Use of AI and AI-Assisted Technologies

AI tool 'Co Pilot' has been used for English language check/correction only.

References

1. Abd-Elaziem, W.; Darwish, M.A.; Hamada, A.; et al. Titanium-Based alloys and composites for orthopedic implants Applications: A comprehensive review. *Mater. Des.* **2024**, *241*, 112850. https://doi.org/10.1016/j.matdes.2024.112850.
2. Voisin, T.; Monchoux, J.P.; Couret, A. Near-Net Shaping of Titanium-Aluminum Jet Engine Turbine Blades by SPS. In *Spark Plasma Sintering of Materials*; Springer International Publishing: Cham, Switzerland, 2019; pp. 713–737. https://doi.org/10.1007/978-3-030-05327-7_25.
3. Singh, N.; Hameed, P.; Ummethala, R.; et al. Selective laser manufacturing of Ti-based alloys and composites: Impact of process parameters, application trends, and future prospects. *Mater. Today Adv.* **2020**, *8*, 100097. https://doi.org/10.1016/j.mtadv.2020.100097.
4. Li, Y.; Wang, X.; Yang, S.; et al. Investigation on Wear Behavior of Cryogenically Treated Ti-6Al-4V Titanium Alloy under Dry and Wet Conditions. *Materials* **2019**, *12*, 2850. https://doi.org/10.3390/ma12182850.
5. Williams, J.C.; Boyer, R.R. Opportunities and Issues in the Application of Titanium Alloys for Aerospace Components. *Metals* **2020**, *10*, 705. https://doi.org/10.3390/met10060705.
6. Arcieri, E.V.; Baragetti, S.; Božić, Ž. Failure analysis of Ti6Al4V titanium alloy under fatigue loading: An experimental and numerical study. *Eng. Fail. Anal.* **2024**, *164*, 108715. https://doi.org/10.1016/j.engfailanal.2024.108715.
7. Lalegani Dezaki, M.; Serjouei, A.; Zolfagharian, A.; et al. A review on additive/subtractive hybrid manufacturing of directed energy deposition (DED) process. *Adv. Powder Mater.* **2022**, *1*, 100054. https://doi.org/10.1016/j.apmate.2022.100054.
8. Frazier, W.E. Metal Additive Manufacturing: A Review. *J. Mater. Eng. Perform.* **2014**, *23*, 1917–1928. https://doi.org/10.1007/s11665-014-0958-z.
9. Khan, P.A.; Raheem, A.; Kalirajan, C.; et al. *In Vivo* Assessment of a Triple Periodic Minimal Surface Based Biomimmetic Gyroid as an Implant Material in a Rabbit Tibia Model. *ACS Mater. Au* **2024**, *4*, 479–488. https://doi.org/10.1021/acsmaterialsau.4c00016.
10. Song, B.; Zhao, X.; Li, S.; et al. Differences in microstructure and properties between selective laser melting and traditional manufacturing for fabrication of metal parts: A review. *Front. Mech. Eng.* **2015**, *10*, 111–125. https://doi.org/10.1007/s11465-015-0341-2.
11. Herzog, D.; Seyda, V.; Wycisk, E.; et al. Additive manufacturing of metals. *Acta Mater.* **2016**, *117*, 371–392. https://doi.org/10.1016/j.actamat.2016.07.019.
12. Gokuldoss, P.K.; Kolla, S.; Eckert, J. Additive Manufacturing Processes: Selective Laser Melting, Electron Beam Melting and Binder Jetting—Selection Guidelines. *Materials* **2017**, *10*, 672. https://doi.org/10.3390/ma10060672.
13. Prashanth, K.G.; Scudino, S.; Klauss, H.J.; et al. Microstructure and mechanical properties of Al–12Si produced by selective laser melting: Effect of heat treatment. *Mater. Sci. Eng. A* **2014**, *590*, 153–160. https://doi.org/10.1016/j.msea.2013.10.023.
14. Scudino, S.; Unterdörfer, C.; Prashanth, K.G.; et al. Additive manufacturing of Cu–10Sn bronze. *Mater. Lett.* **2015**, *156*, 202–204. https://doi.org/10.1016/j.matlet.2015.05.076.
15. Wang, Z.; Tang, S.Y.; Scudino, S.; et al. Additive manufacturing of a martensitic Co–Cr–Mo alloy: Towards circumventing the strength–ductility trade-off. *Addit. Manuf.* **2021**, *37*, 101725. https://doi.org/10.1016/j.addma.2020.101725.
16. Prashanth, K.G.; Debalina, B.; Wang, Z.; et al. Tribological and corrosion properties of Al–12Si produced by selective laser melting. *J. Mater. Res.* **2014**, *29*, 2044–2054. https://doi.org/10.1557/jmr.2014.133.
17. Prashanth, K.G.; Scudino, S.; Chaubey, A.K.; et al. Processing of Al–12Si–TNM composites by selective laser melting and evaluation of compressive and wear properties. *J. Mater. Res.* **2016**, *31*, 55–65. https://doi.org/10.1557/jmr.2015.326.
18. Bartolomeu, F.; Faria, S.; Carvalho, O.; et al. Predictive models for physical and mechanical properties of Ti6Al4V produced by Selective Laser Melting. *Mater. Sci. Eng. A* **2016**, *663*, 181–192. https://doi.org/10.1016/j.msea.2016.03.113.
19. Molinari, A.; Straffelini, G.; Tesi, B.; et al. Dry sliding wear mechanisms of the Ti6Al4V alloy. *Wear* **1997**, *208*, 105–112. https://doi.org/10.1016/s0043-1648(96)07454-6.
20. Attar, H.; Prashanth, K.G.; Chaubey, A.K.; et al. Comparison of wear properties of commercially pure titanium prepared by selective laser melting and casting processes. *Mater. Lett.* **2015**, *142*, 38–41. https://doi.org/10.1016/j.matlet.2014.11.156.
21. Sieniawski, J.; Ziaja, W.; Kubiak, K.; et al. Microstructure and Mechanical Properties of High Strength Two-Phase Titanium Alloys. In *Titanium Alloys—Advances in Properties Control*; InTech: Houston, TX, USA, 2013. https://doi.org/10.5772/56197.

22. He, J.; Li, D.; Jiang, W.; et al. The Martensitic Transformation and Mechanical Properties of Ti6Al4V Prepared via Selective Laser Melting. *Materials* **2019**, *12*, 321. https://doi.org/10.3390/ma12020321.
23. Karimi, J.; Zhao, C.; Prashanth, K.G. Massive transformation in dual-laser powder bed fusion of Ti6Al4V alloys. *J. Manuf. Process.* **2024**, *119*, 282–292. https://doi.org/10.1016/j.jmapro.2024.03.083.
24. Karimi, J.; Suryanarayana, C.; Okulov, I.; et al. Selective laser melting of Ti6Al4V: Effect of laser re-melting. *Mater. Sci. Eng. A* **2021**, *805*, 140558. https://doi.org/10.1016/j.msea.2020.140558.
25. Agius, D.; Kourousis, K.I.; Wallbrink, C.; et al. Cyclic plasticity and microstructure of as-built SLM Ti-6Al-4V: The effect of build orientation. *Mater. Sci. Eng. A* **2017**, *701*, 85–100. https://doi.org/10.1016/j.msea.2017.06.069.
26. Agius, D.; Kourousis, K.I.; Wallbrink, C. A Review of the As-Built SLM Ti-6Al-4V Mechanical Properties towards Achieving Fatigue Resistant Designs. *Metals* **2018**, *8*, 75. https://doi.org/10.3390/met8010075.
27. Zhao, C.; Wang, Z.; Li, D.; et al. Cu-Ni-Sn alloy fabricated by melt spinning and selective laser melting: A comparative study on the microstructure and formation kinetics. *J. Mater. Res. Technol.* **2020**, *9*, 13097–13105. https://doi.org/10.1016/j.jmrt.2020.09.047.
28. Jung, H.Y.; Choi, S.J.; Prashanth, K.G.; et al. Fabrication of Fe-based bulk metallic glass by selective laser melting: A parameter study. *Mater. Des.* **2015**, *86*, 703–708. https://doi.org/10.1016/j.matdes.2015.07.145.
29. Thijs, L.; Verhaeghe, F.; Craeghs, T.; et al. A study of the microstructural evolution during selective laser melting of Ti–6Al–4V. *Acta Mater.* **2010**, *58*, 3303–3312. https://doi.org/10.1016/j.actamat.2010.02.004.
30. Wang, D.; Chen, X.; Li, F.; et al. Influence of normal load, electric current and sliding speed on tribological performance of electrical contact interface. *Microelectron. Reliab.* **2023**, *142*, 114929. https://doi.org/10.1016/j.microrel.2023.114929.
31. Grejtak, T.; Gallego, N.C.; Arregui-Mena, J.D.; et al. Sliding friction and wear behavior of nuclear graphite in high temperature inert environment: Influence of contact load, speed and temperature. *Wear* **2026**, *599*, 206779. https://doi.org/10.1016/j.wear.2026.206779.
32. Stott, F.H. High-temperature sliding wear of metals. *Tribol. Int.* **2002**, *35*, 489–495. https://doi.org/10.1016/s0301-679x(02)00041-5.
33. Du, D.H.; Yu, Z.J.; Tao, F.J.; et al. Effect of softening in near-surface region on wear transition of Ti-6Al-4V alloy at elevated temperatures. *IOP Conf. Ser. Mater. Sci. Eng.* **2021**, *1167*, 012014. https://doi.org/10.1088/1757-899x/1167/1/012014.
34. Gowda, H.D.S.; Hemaraju; Kumar, V.G.P.; et al. Optimizing abrasive wear in sustainable MCC reinforced hemp bamboo epoxy composites for tribological applications. *Sci. Rep.* **2026**, *16*, 12990. https://doi.org/10.1038/s41598-026-43505-9.
35. Hokkirigawa, K.; Kato, K. An experimental and theoretical investigation of ploughing, cutting and wedge formation during abrasive wear. *Tribol. Int.* **1988**, *21*, 51–57. https://doi.org/10.1016/0301-679x(88)90128-4.
36. Pirso, J.; Viljus, M.; Juhani, K.; et al. Three-body abrasive wear of TiC–NiMo cermets. *Tribol. Int.* **2010**, *43*, 340–346. https://doi.org/10.1016/j.triboint.2009.06.014.
37. Valizade, N.; Farhat, Z. A Review on Abrasive Wear of Aluminum Composites: Mechanisms and Influencing Factors. *J. Compos. Sci.* **2024**, *8*, 149. https://doi.org/10.3390/jcs8040149.
38. So, H. The mechanism of oxidational wear. *Wear* **1995**, *184*, 161–167. https://doi.org/10.1016/0043-1648(94)06569-1.
39. Dong, C.; Yuan, C.; Bai, X.; et al. Coupling mechanism between wear and oxidation processes of 304 stainless steel in hydrogen peroxide environments. *Sci. Rep.* **2017**, *7*, 2327. https://doi.org/10.1038/s41598-017-02530-5.
40. Liu, Y.; Bai, X.; Cheng, K. A study on the formation of wear debris during abrasion. *Tribol. Int.* **1985**, *18*, 107–111. https://doi.org/10.1016/0301-679x(85)90047-7.
41. Jahanmir, S.; Suh, N.P.; Abrahamson, E.P. The delamination theory of wear and the wear of a composite surface. *Wear* **1975**, *32*, 33–49. https://doi.org/10.1016/0043-1648(75)90203-3.
42. Söderman, A.; Törnquist, P.L. Galling is a serious issue in many industries that use stainless steel fasteners- but there are solutions. *Met. Powder Rep.* **2021**, *76*, 194–195. https://doi.org/10.1016/j.mrpr.2019.07.004.
43. Devenport, T.M.; Griffin, J.M.; Rolfe, B.F.; et al. Friction and Wear in Stages of Galling for Sheet Metal Forming Applications. *Lubricants* **2023**, *11*, 288. https://doi.org/10.3390/lubricants11070288.
44. Finkin, E.F. Adhesive wear: A general review of the state of experimental knowledge and theory. *Int. J. Mater. Eng. Appl.* **1979**, *1*, 154–161. https://doi.org/10.1016/0141-5530(79)90004-9.
45. Fleming, J.R.; Suh, N.P. Mechanics of crack propagation in delamination wear. *Wear* **1977**, *44*, 39–56. https://doi.org/10.1016/0043-1648(77)90083-7.
46. Meng, X.; Lin, Y.; Mi, S.; et al. The Study of Tool Wear Mechanism Considering the Tool–Chip Interface Temperature during Milling of Aluminum Alloy. *Lubricants* **2023**, *11*, 471. https://doi.org/10.3390/lubricants11110471.
47. Pan, S.; Li, C.; Zhu, W.; et al. Establishment of an improved wear model for high-temperature contact interfaces and investigation of wear behavior. *Wear* **2026**, *602*, 206914. https://doi.org/10.1016/j.wear.2026.206914.
48. Palanikumar, P.; Gnanasekaran, N.; Subrahmanya, K.; et al. Effect of sliding speed and rise in temperature at the contact interface on coefficient of friction during full sliding of SS304. *Mater. Today Proc.* **2020**, *27*, 1996–1999. https://doi.org/10.1016/j.matpr.2019.09.046.

49. Waterhouse, R.B.; Taylor, D.E. Fretting debris and the delamination theory of wear. *Wear* **1974**, *29*, 337–344. https://doi.org/10.1016/0043-1648(74)90019-2.
50. Han, L.; Qi, H. Dynamic response analysis of helical gear pair considering the interaction between friction and mesh stiffness. *Meccanica* **2019**, *54*, 2325–2337. https://doi.org/10.1007/s11012-019-01088-y.
51. Tang, B.; Wu, P.Q.; Fan, A.L.; et al. Improvement of Corrosion-Wear Resistance of Ti-6Al-4V Alloy by Plasma Mo-N Surface Modification. *Adv. Eng. Mater.* **2005**, *7*, 232–238. https://doi.org/10.1002/adem.200400207.